Experimental characterisation of breaking wave impact loads on a vertical cylinder

Florian Hulin, Alan Tassin, Jean-François Filipot, Nicolas Jacques

Experimental characterisation of breaking wave impact loads on a vertical cylinder

Florian Hulin[1, 2, 3]†, Alan Tassin[2], Jean-François Filipot[1] and Nicolas Jacques[3]

[1]France Énergies Marines, Plouzané, France

[2]Ifremer, RDT, F-29280 Plouzané, France

[3]ENSTA Bretagne, UMR CNRS 6027, IRDL, 29806 Brest Cedex 09, France

(Received xx; revised xx; accepted xx)

This article presents experimental measurements of breaking wave impact loads on a vertical cylinder. The focus is on the influence of some of the breaking wave properties on the measured force. These properties are the distance to breaking, δ, defined as the distance between the breaking location and the front face of the cylinder, and the breaking strength, characterised here by the Γ parameter proposed by Derakhti *et al.* (2018). The wave characteristics are obtained through numerical simulations of the breaking waves using a fully non-linear potential flow solver. Seven breaking waves with different breaking strengths have been considered. For each wave, the distance to breaking has been systematically varied and the resulting impact force time-history was measured. It is found that except for the two less intense breaking cases, corresponding to values of Γ lower than one, there is a value of δ for which the magnitude of the impact force is maximum. Small variations of the distance to breaking δ strongly influence the impact force time-history and its maximum. A linear relationship is observed between the maximum force and the breaking strength Γ. For the wave cases with values of Γ higher than one, the maximum impact force is observed when the distance to breaking δ is close to 5 % of the wavelength. An empirical wave slamming coefficient accounting for the distance to breaking δ and the breaking strength Γ is derived.

Key words: Authors should not enter keywords on the manuscript, as these must be chosen by the author during the online submission process and will then be added during the typesetting process (see Keyword PDF for the full list). Other classifications will be added at the same time.

† Email address for correspondence: florian.hulin@ec-nantes.fr

1. Introduction

Offshore structures such as floating offshore wind turbines (FOWTs) are exposed to harsh environments that may threaten their integrity. The highest hydrodynamic loads encountered by these structures are often due to the hydrodynamic impact of breaking waves (Paulsen *et al.* 2019). The associated peak loads may be twice the loads generated by non-breaking waves with an equivalent height (Kjeldsen *et al.* 1986; Paulsen *et al.* 2019). Moreover, slamming loads are impulsive and they may trigger a dynamic response of the impacted structure at its first modes (Suja-Thauvin *et al.* 2017). In spite of the different studies dedicated to breaking wave impacts, it is still challenging to predict accurately the loads that may be induced by breaking waves.

Because of the complexity of the flows taking place in breaking waves interacting with offshore structures (e.g., three-dimensional effects), analytical approaches based on slamming models (Goda *et al.* 1966; Wienke & Oumeraci 2005) only provide an estimate of the maximum force that may occur during a breaking wave impact. Indeed, despite some recent efforts to improve this kind of models using more realistic impact conditions in terms of free-surface profile and fluid kinematics at the instant of impact (Renaud *et al.* 2023; Tai *et al.* 2024), it remains hard to predict accurately the force time-history during an impact. Simplified models are nevertheless very useful for a quick, and in general conservative, estimate of the maximum force that may be induced by a breaking wave impact. For a detailed prediction of the force time-history induced by a particular breaking wave and a certain distance to breaking, one has to rely on high-fidelity numerical simulations (e.g., Paulsen *et al.* 2014; Batlle Martin *et al.* 2023). However, the high computational cost associated to these approaches limits their use to the impact of a few waves, while the design process of an offshore structure requires to simulate a large number of waves to achieve robust load statistics. As a consequence, breaking wave impact forces are often studied through experimental investigations, which also have their own limitations and difficulties. A first difficulty is due to the impulsive nature of wave impacts: the dynamic response of the model triggered by the impact will induce oscillations of the force or pressure measurements. Even though several methods have been developed to address this issue (e.g., Wienke & Oumeraci 2005; Alsalah *et al.* 2021; Antonini *et al.* 2021; Tassin *et al.* 2024), it still limits the precision of the force measurements. Moreover, an intrinsic low repeatability of the wave impact phenomenon has also been reported. This low repeatability can be illustrated by the force measurements of the same wave impact case carried out by Ha *et al.* (2020), for which they observed significant variations in terms of magnitude of the impact force, starting time of the impact and characteristics of the time history (see their figure 7). Moalemi *et al.* (2024) showed that this variability was linked to the variability of the wave shape at impact. By regrouping the impact cases for which the wave heights and slopes before the impact were similar, they managed to reduce the variability observed on the force measurements. Another difficulty that arises when studying breaking wave impacts is the identification of the slamming contribution in the force measurements. Experiments are often carried out to determine or validate slamming formulas, which aim to predict the slamming term of the force. However, the measured force also contains a "Morison term", which is not due to slamming. Different approaches have been proposed (e.g. Wienke & Oumeraci 2005; Ghadirian *et al.* 2023) to extract the slamming

contribution from the force measurement. They all rely on strong assumptions and there is no widely accepted approach. One last difficulty is the characterisation of the impacting wave. As pointed out by Moalemi *et al.* (2024), the wave shape before the impact considerably affects the impact loads. In many experiments, the only accessible wave data are local wave height measurements obtained from wave gauges (e.g., Suja-Thauvin *et al.* 2017; Paulsen *et al.* 2019), or free-surface profile measurements at the side of the wall obtained from high-speed video cameras (e.g., Ma *et al.* 2020; Ha *et al.* 2020). Local wave height measurements do not allow to access the free-surface profile at impact and are often limited to the computation of the wave height, period and local time derivative. Video camera measurements allow to obtain the spatial free-surface profile. They are however limited to flumes presenting a side glass wall, and the accuracy of the measurements is affected by the modification of the wave by the wall (Rapp & Melville 1990), in particular close to the instant of breaking.

In spite of these difficulties, experimental approaches are commonly used to study the loads generated by breaking wave impacts. Their results are also crucial for the validation of numerical simulations. Most of these experiments aim to derive formulas that link the characteristics of a given wave or sea-state to the impact force it may generate on a cylinder. This is often achieved by empirically modifying a theoretical impact formula based on experimental measurements (Goda *et al.* 1966; Tanimoto *et al.* 1987; Wienke & Oumeraci 2005; Paulsen *et al.* 2019). All the aforementioned studies propose to write the time evolution of the slamming term of the force as:

$$F_S(t) = f(t)\beta\rho c^2 R\eta_b, \tag{1.1}$$

where η_b is the height of the crest of the breaking wave, c the crest speed, R the radius of the cylinder, ρ the density of the fluid, $f(t)$ a normalized time function and β a dimensionless coefficient. The main difference between the different approaches lies in the choice of the time history function, $f(t)$, and of the value of the coefficient β. In many studies, β corresponds to the product of a slamming coefficient C_S and a curling factor λ (Goda *et al.* 1966; Wienke & Oumeraci 2005; Paulsen *et al.* 2019). The curling factor was initially defined as the percentage of the wave crest which is vertical and which impacts the mockup (Goda *et al.* 1966). Over the height $\lambda\eta_b$, analytical impact formulas such as the ones proposed by von Karman (1929) and Wagner (1932) are usually applied. In later studies, other definitions were proposed for the curling factor. Wienke & Oumeraci (2005) adjusted the curling factor so as to obtain a good agreement between theory and experiments. Paulsen *et al.* (2019) defined it as the base of a triangular shaped pressure distribution along the cylinder. The curling factor is related to the strength of the breaking wave: the more severe the breaking wave, the higher the curling factor. However, quantifying the strength of a breaking wave is not an easy task and different approaches have been adopted: Goda *et al.* (1966) recommended two different curling factor values, one for plunging waves and one for spilling waves; Sawaragi & Nochino (1984) and Tanimoto *et al.* (1987) proposed a quantification of the breaking strength based on the slope of the bottom of the flume (thus only valid for bathymetric breaking waves). It appears from these approaches that no robust methodology has been proposed to account for the severity of the breaking wave.

Other experimental works focused on assessing the importance of the distance δ between the cylinder and the breaking location for the impact load. Zhou *et al.*

(1991) and Manjula *et al.* (2013) reported that the time history and magnitude of the pressure measured on the surface of a cylinder strongly depend on the position of the cylinder with respect to the breaking location. Ma *et al.* (2020) reported variations of 50 % of the magnitude of the impact force depending on the location of the cylinder while Sawaragi & Nochino (1984) observed variations of more than 600 %. Other works indirectly studied the influence of the distance to breaking δ by investigating different wave shapes at impact (e.g., Moalemi *et al.* 2024; Zhang *et al.* 2024): the impact of a wave that just overturned corresponds to a close-to-zero δ value, while the impact of a fully overturned wave corresponds to a high value of δ. To the best of the author's knowledge, the only studies that quantitatively related the distance to breaking to the impact force are the ones by Sawaragi & Nochino (1984) and by Ma *et al.* (2020). This lack of quantification may be due to the earlier mentioned difficulty of determining the breaking location in experiments. Sawaragi & Nochino (1984) determined it as the first position at which bubbles appeared, and Ma *et al.* (2020) used a high-speed video camera to measure the wave profile through a glass wall. Until now, no impact load formula accounting for this distance has been proposed. This inability to account for the stage of breaking at impact is likely to explain the low correlation between the shape of a breaking wave and the magnitude of the induced impact force that has been reported in some studies focusing on wave impact loads in irregular sea states. For instance, Paulsen *et al.* (2019) investigated the influence of the height and period of a breaking wave on the magnitude of the impact force by measuring the force acting on a surface piercing vertical cylinder exposed to a breaking irregular sea state. They observed that "*it is not necessarily the highest nor the steepest waves which are causing the largest impact forces*". Similarly, Guo *et al.* (2020) observed a rather low correlation between the height, period and crest velocity of breaking waves with the impact forces measured on a semi-submersible platform at basin scale. To explain this low correlation, Paulsen *et al.* (2019) speculated that "*the point of breaking relative to the cylinder could be of particular importance for the magnitude of the impact force*". Indeed, according to the works focusing on the importance of the distance between the cylinder and the breaking location, a strong breaking wave could generate an impact force gentler than a mild breaking wave depending on the breaking stage at impact.

In the present study, we experimentally investigate the combined effect of the breaking strength and location on the impact force measured on a vertical cylinder. The force oscillation issue is addressed through the approach recently proposed by Tassin *et al.* (2024). The free-surface profile of the different waves was precisely obtained with a fully non-linear potential flow (FNPF) solver (Grilli *et al.* 1989; Grilli & Subramanya 1996). In particular, this allowed to determine the "breaking location", which is here defined as the location at which the free surface first becomes locally vertical. These simulations and the use of a motion generator on which the mockup was fixed allowed to precisely characterise the evolution of the magnitude of the impact force with the distance between the breaking point and the cylinder. A quantitative characterisation of the breaking strength is achieved by computing the parameter Γ proposed by Derakhti *et al.* (2018) using the FNPF simulations. The Γ parameter is defined as:

$$\Gamma = T_b \frac{\mathrm{d}B}{\mathrm{d}t}\bigg|_{B=0.85}, \tag{1.2}$$

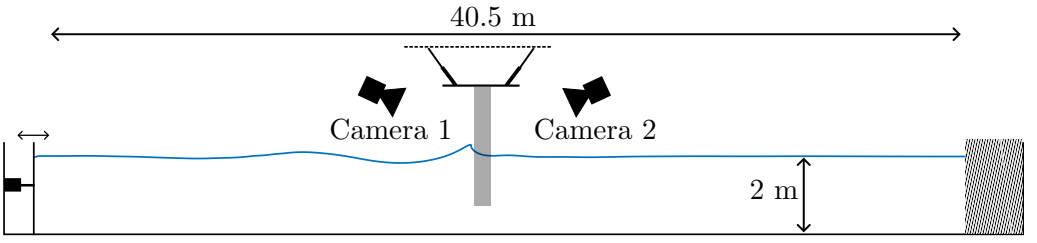

Figure 1: Scheme of the wave flume with the mockup and the high-speed video cameras.

where T_b is a characteristic wave period and $B = u/c$ is the ratio between the horizontal fluid velocity at the crest, u, and the crest velocity, c. Derakhti *et al.* (2018) showed that the energy dissipated during a breaking event is strongly correlated to the value of Γ.

The article is structured as follows. Section 2 describes the experimental approach and introduces different quantities used for the analysis of the results. Section 3 describes the generation and characterisation of the breaking waves. Section 4 presents impact-force time-histories measured for different impact conditions. The influence of the impact conditions on the magnitude of the impact force is analysed in section 5. The effect of the breaking strength, characterised by the Γ parameter, and of the distance to breaking δ is investigated. Eventually, an empirical formula for the magnitude of the impact force that accounts for δ and Γ is introduced in section 6. Based on this formula, a wave slamming coefficient depending on δ and Γ is proposed. Conclusions are drawn in section 7.

2. Experimental approach

In this section, the experimental set-up and protocol are presented. The experimental facility and the mockup are presented in section 2.1. The methodology applied to compensate for the force oscillations induced by the vibrations of the model is described in section 2.2. In section 2.3, we define the physical quantities used later to analyse the results.

2.1. *Experimental set-up*

The experiments were carried out in the wave flume of Ifremer, Brest. A schematic description of the flume is depicted in figure 1. The experimental flume is 40.5 m long from the wave generator to the absorbing beach, 4 m wide and 2 m deep. It is equipped with a piston-type wave generator. The mockup was fixed on a motion generator of type Mistral manufactured by Symétrie that allowed to accurately control the location of the mockup. Two high-speed video cameras were installed on the side of the flume to film the front and rear faces of the mockup during the wave impacts. The video cameras trigger was synchronised with the motion of the wave generator.

A segmented mockup, of which a schematic view is depicted in figure 2, was used to measure independently the forces acting on different portions of the cylinder (sections S_1 to S_4 in figure 2). The mockup is a 1.81 m high circular cylinder with a diameter of 40 cm. As shown in the cross-sectional view displayed in figure 3a, the cylinder is composed of six sections, out of which 4 are instrumented (sections S_1 to S_4). Each instrumented section is composed of an outer part, called the

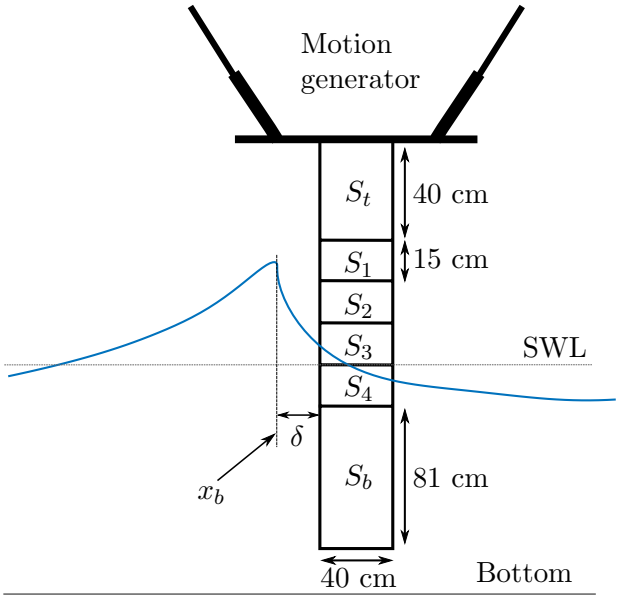

Figure 2: Description of a breaking wave impacting the mockup in the flume. Parameter δ corresponds to the distance between the breaking location and the front face of the cylinder. The vertical dashed line indicates the breaking location x_b and the horizontal dotted line the still water level (SWL).

skin element, and an inner part, called the backbone element. These two parts are visible in the exploded view depicted in figure 3b. The skin and backbone elements are linked through a load cell (of type MCS10-025 for sections S_1, S_2 and S_3 and of type MCS10-010 for section S_4). The signals of the load cells were recorded at a sample frequency of 250 kHz. Waterproofness of the mockup was ensured using surgical tape filling in the 3 mm gap between the different sections. The mockup was positioned so that the intersection between sections S_4 and S_3 lies at the still water level (SWL).

The present set-up allows to modify the distance to breaking, δ, by changing the location of the cylinder, and not the breaking location of the wave as it has been done by some authors in the past (e.g., Wienke & Oumeraci 2005). Therefore, it is certain that the results obtained for different values of δ correspond to the impact of the same wave.

2.2. *Compensation of the vibration induced force oscillations*

During the impact of a breaking wave, different modes of the skin elements can be excited. This induces oscillations of the force signals that complicate the interpretation of the force measurements. In order to compensate for these oscillations, we applied the methodology proposed by Tassin *et al.* (2024). In the aforementioned study, the present set-up was used as a case study to demonstrate the efficiency of the method. The results were limited to the upper section. Given that the methodology is detailed in Tassin *et al.* (2024), we only recall the main assumptions of the method and we present the instrumentation used for the different sections.

The compensation methodology consists in recording the dynamic response of the impacted structure to estimate the part of the measured force that is

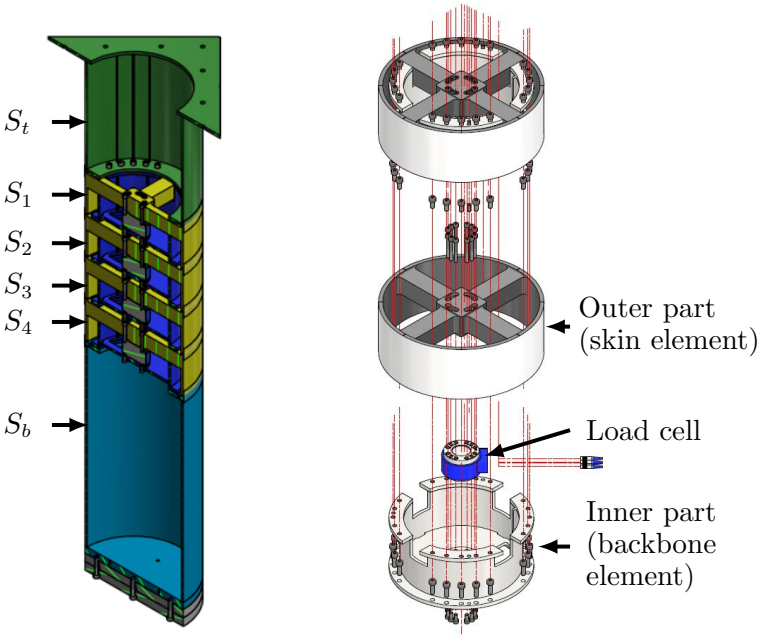

(a) Cross-sectional view of the mockup

(b) Exploded view of two instrumented sections

Figure 3: Description of the mockup

induced by the structural response. The response is recorded by acceleration measurements at different points of the structure. Correction coefficients that were priorly computed from hammer tests allow to estimate the influence of the structural response on the force signal as the sum of the acceleration signals multiplied by the coefficients, and to subtract it from the raw measurement. With this methodology, we obtain an acceptable level of residual oscillations without loosing the high-frequency content of the force signal (that would have been removed by a simple low-pass filter).

The number and locations of the accelerometers used for the present experiments are detailed in figure 4. Six accelerometers were placed on the upper section S_1 that is the one experiencing the most violent impacts, 5 were placed on section S_2, and one accelerometer per section was placed on sections S_3 and S_4 that were not impacted by the waves and experienced a limited level of oscillations. Similarly to the load cells, the accelerometers signals were recorded with a sampling frequency of 250 kHz. The number of accelerometers placed on a section determines the number of modes of the section that can be compensated for. For this reason, we filtered out the very high frequency content of the acceleration and force signals that is due to higher frequency modes. The force oscillations induced by these modes cannot be compensated for given the number of accelerometers used in the experiments. The signals recorded on section S_1 were low-pass filtered at 1000 Hz, the ones on section S_2 at 700 Hz and the ones on sections S_3 and S_4 at 300 Hz. Comparisons of the filtered and non-filtered frequency contents presented in Hulin (2024) show that these cut-off frequencies allow to retain most of the

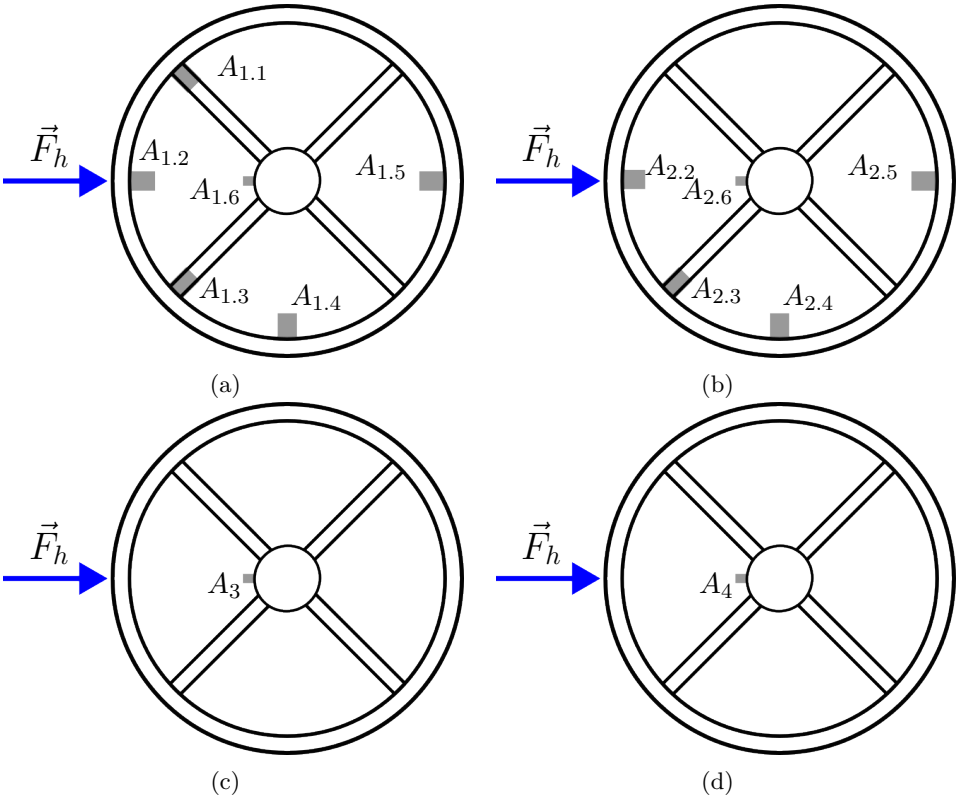

Figure 4: Accelerometer configuration for the complete set-up: top view of the skin elements for sections S_1 (a), S_2 (b), S_3 (c) and S_4 (d).

force frequency content. More details, in particular concerning the computation of the compensation coefficients, are also given in Hulin (2024).

2.3. *Definition of physical quantities of interest for the present study*

In this section, we define different physical quantities that are used throughout the study.

The breaking location, x_b, is defined as the location at which the free surface of the wave becomes locally vertical for the first time. We call the instant at which this event occurs the breaking time, t_b. In figure 2, the blue profile corresponds to a wave profile at the instant t_b. The breaking location, x_b, is indicated by the vertical dashed line. The distance between the breaking location and the front face of the cylinder, also shown in figure 2, is denoted by δ. This distance is non-dimensionalised as $\bar{\delta} = \delta/L$, where L is the characteristic wavelength of the wave spectrum (see table 1). Here, L is computed as the wavelength linked to the peak period T_p of the spectrum through the linear dispersion relation ($L = \frac{gT_p^2}{2\pi}\tanh(\frac{2\pi h}{L})$, where h is the water depth).

Following seminal analytical approaches, the force F acting on a cylinder during a wave impact may be written as the sum of a drag term F_D, an inertial term F_I and a slamming term F_S (Goda *et al.* 1966; Wienke & Oumeraci 2005):

$$F = F_D + F_I + F_S. \tag{2.1}$$

However, as mentioned in the introduction, extracting the slamming term F_S from the total hydrodynamic force is not straightforward. As a consequence, many authors studied the hydrodynamic force acting on the whole cylinder (e.g. Wienke & Oumeraci 2005; Paulsen *et al.* 2019; Ma *et al.* 2020). Different possibilities were investigated by Ghadirian *et al.* (2023) to extract the impact term from the total hydrodynamic force obtained from numerical simulations. They observed that the different methods lead to rather different estimates of the slamming term. Moreover, some of the methods depend on the value of the first or even second time-derivative of the force and may not be applicable to experimental measurements affected by measurement noise. Sawaragi & Nochino (1984) approximated the impact force as the force acting above the SWL. This was permitted by the use of a segmented mockup. Even though a part of the hydrodynamic force acting above the SWL is due to the non-impulsive terms, this definition has the advantage of being simple, unambiguous and applicable to experimental and numerical results. In the present study, we followed the approach of Sawaragi & Nochino (1984): we study the influence of the different impact conditions on the force F_{SWL} acting above the SWL. It corresponds to the force acting on the three upper sections S_1, S_2 and S_3 (see figure 2). Another possibility would have been to study the force acting on the two upper sections, where the impact occurs. However, with this approach, the percentage of the wave height accounted for in the impact force would depend on the height of the wave. Moreover, non-impulsive terms would still be present in the measurements.

Also, following Sawaragi & Nochino (1984), we define the non-dimensional impact force $\bar{F}_{SWL}$ as:

$$\bar{F}_{SWL} = \frac{F_{SWL}}{\pi\rho c^2 R\eta_b}, \tag{2.2}$$

where R is the radius of the cylinder, ρ the density of water, c the wave crest celerity and η_b the wave crest height. The quantity $\pi\rho c^2 R\eta_b$ corresponds to the theoretical maximum impact force acting on a cylinder of length η_b entering calm water at speed c derived from the theory of von Karman (1929). Note that the non-dimensional impact force, $\bar{F}_{SWL}$, may be interpreted as the curling factor λ introduced by Goda *et al.* (1966) which represents the percentage of the wave crest that is impacting the cylinder. Indeed, following Goda's theory, the maximum slamming force is equal to $F_S = \lambda\pi\rho c^2 R\eta_b$. The difference between $\bar{F}_{SWL}$ and λ lies in the fact that $\bar{F}_{SWL}$ includes a non-impulsive term, while $\bar{F}_S = \lambda$ is the slamming term of the non-dimensional force.

3. Breaking waves generation and characterisation

The breaking waves were generated through the focusing of wave packets defined with a JONSWAP spectrum, using the iterative procedure detailed in Hulin *et al.* (2025). The iterative procedure was applied to obtain breaking close to $x_t = 21$ m. Note that, in contrast to the work presented in Hulin *et al.* (2025), the focusing time was selected as $t_f = 30$ s. During the experimental campaign, seven breaking wave cases were used. The parameters of the spectrum used for the wave generation are given in table 1. The significant wave height, H_S, of the spectra was varied to obtain different breaking strengths, i.e. different values of Γ. The peak period, T_p, was also varied to vary the wavelength, i.e. the scale, of the breaking waves. The focusing location results from the iterative procedure, and

Wave Number	H_S [m]	T_p [s]	γ [1]	f_c [Hz]	Δf [Hz]	x_f [m]	t_f [s]	L [m]
1	0.12	2.25	3.3	0.8	0.01	18.80	30	7.39
2	0.13	2.25	3.3	0.8	0.01	22.99	30	7.39
23	0.135	2.25	3.3	0.8	0.01	23.57	30	7.39
24	0.14	2.25	3.3	0.8	0.01	23.87	30	7.39
3	0.15	2.25	3.3	0.8	0.01	24.15	30	7.39
7	0.13	2.49	1.4	0.8	0.01	19.69	30	8.67
15	0.10	2.0	3.3	0.9	0.01	23.40	30	6.05

Table 1: List of the parameters used to generate the breaking waves for the experimental campaign. The parameters of the JONSWAP spectrum are the significant wave height, H_S, the peak period, T_p, the peak enhancement factor, γ, the cut-off frequency, f_c, and the frequency discretization, Δf. Parameters x_f and t_f correspond to the focusing location and time, respectively. Parameter L is the wavelength linked to the peak period T_p through the linear dispersion relation.

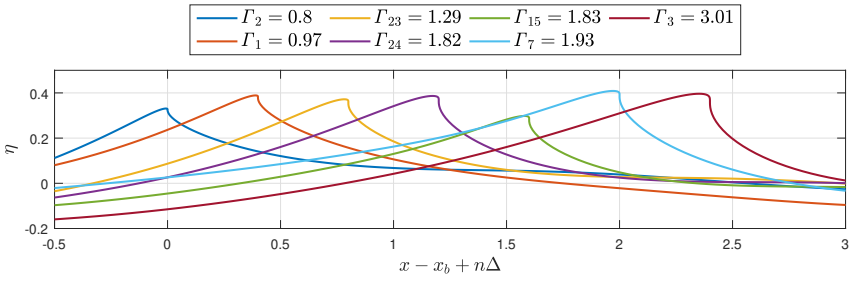

Figure 5: Numerical free-surface profiles at the instant of breaking of the waves listed in table 1. The waves are ordered by increasing values of Γ and the index corresponds to the wave number (given in table 1). To improve the readability of the figure, the profiles were shifted in space so that the breaking location corresponds to $n\Delta$, where n is an integer and $\Delta = 0.4$ m.

the wavelength L is computed as the wavelength associated to the peak period of the spectrum, T_p, through the linear dispersion relation ($L = \frac{gT_p^2}{2\pi}\tanh(\frac{2\pi h}{L})$, where h is the water depth).

The different breaking waves were modelled using the FNPF solver based on the boundary element method proposed by Grilli *et al.* (1989); Grilli & Subramanya (1996). Notice that a validation of this numerical model through comparisons with experimental free-surface profiles was performed by Hulin *et al.* (2025). The free-surface profiles of the 7 waves listed in table 1 are shown in figure 5. The waves are ordered by increasing values of Γ and are shown at the instant of breaking. To improve the readability, the profiles are shifted in the x-direction.

Wave Number	x_b [m]	t_b [s]	η_b [m]	c [m/s]	Γ [1]
1	21.00	30.56	0.39	2.7	0.97
2	21.04	27.25	0.33	2.49	0.8
23	20.99	26.93	0.37	2.74	1.29
24	20.99	26.77	0.39	2.83	1.82
3	20.99	26.58	0.4	2.89	3.01
7	20.97	30.12	0.41	2.85	1.93
15	21.01	27.06	0.3	2.41	1.83

Table 2: Characteristics of the breaking waves used during the experimental campaign.

Visually, it appears that the higher the value of Γ, the higher the curling factor (the percentage of the wave that is "vertical"). The FNPF solver was also used to compute the different parameters of interest of the breaking waves given in table 2: the breaking location, x_b, the instant of breaking, t_b, the crest elevation at the instant of breaking, η_b, the crest speed at the instant of breaking, c, and the breaking strength parameter, Γ. More details on the numerical configuration and the computation of the different wave parameters are given in Hulin *et al.* (2025). The computation of the breaking location, x_b, was used to compute the distance to breaking δ.

In the following sections, we will observe that variations of a few centimetres of the distance to breaking may have a strong influence on the measured force. However, we are not able to assert that the values of x_b listed in table 2 have a centimetric accuracy. Indeed, experimental measurements of x_b are not sufficiently accurate to be used as references to quantify the accuracy of the values of x_b obtained numerically. Nevertheless, as explained in section 2.1, the distance δ was varied by modifying the position of the cylinder with the motion generator. The error on the position of the cylinder is known to be smaller than 1 mm. As a consequence, even if the absolute value of δ may be inaccurate, the variations of δ are very accurate. Thus, the obtained force evolutions as a function of δ are reliable, although the absolute values of δ are not known accurately.

4. Time histories of the impact force for different wave impact conditions

In this section, we present the force measurements obtained for different impact conditions (i.e. different wave cases and locations of the cylinder). We investigate the repeatability of the force measurements in section 4.1 and we present the force measurements obtained for the different impact conditions in section 4.2. The effect of the wave-shape on the characteristics of the force time-history is analysed in section 4.3. The importance of the diffraction of the wave by the cylinder for the force time-history is highlighted in section 4.4. In this section as well as in the following ones, the compensation methodology presented in section 2.2 is applied to the force measurements.

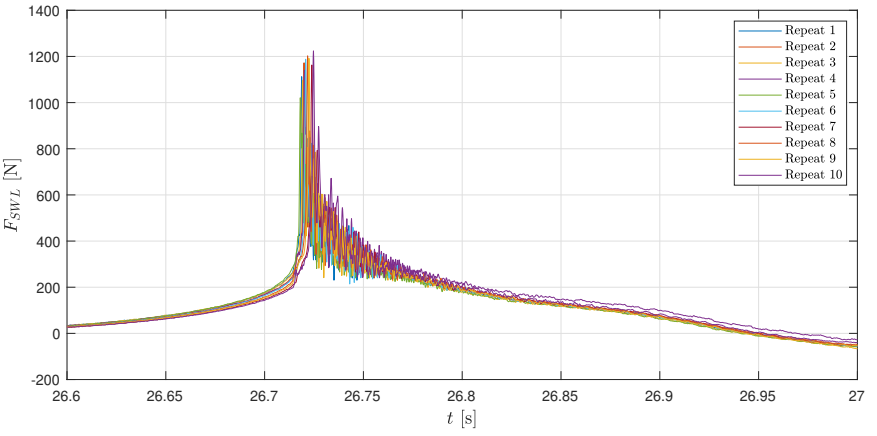

Figure 6: Time-histories of the force F_{SWL} measured during 10 repeats of the impact of wave 3 for $\bar{\delta} = 0.043$.

4.1. *Repeatability of the force measurements*

To assess the repeatability of the experiments, we repeated 10 times the force measurement for the impact of wave 3 at $\bar{\delta} = 0.043$. These impact conditions were chosen because they are among those inducing the strongest loads and the highest levels of oscillations that we observed. As such, they are likely to be among the impact conditions with the lowest repeatability. The force measurements resulting from the ten repeats are depicted in figure 6. The mean value of the maximum impact force for the ten repeats is of 1151 N and it displays a standard deviation of 58 N, which represents 5 % of the mean value of the maximum impact force. It also appears from this figure that the force measurements are time shifted with respect to each other. The largest time shift, measured as the time interval between the force maxima for repeats 5 and 10, is of 7 ms. This high level of repeatability was attained at the cost of a minimum resting time of 45 minutes between two experiments. In the following, the maximum value of the impact force in time will be called "magnitude of the impact force". This term is used to differentiate it from the maximum over δ of the magnitude of the impact force.

4.2. *Force measurements for the different impact conditions*

For the 7 waves listed in table 1, the force F_{SWL} was measured for several distances to breaking δ. The corresponding time evolutions of F_{SWL} are shown in figure 7. Each subfigure corresponds to a wave case and each curve was obtained with a particular distance δ. The legends indicate the corresponding values of $\bar{\delta}$. Note that intermediate $\bar{\delta}$ values, which are not shown in the figure for clarity, were also investigated. Except for waves 1 and 2 that displayed a much smaller variability in the force measurements, the experiments were repeated at least three times for almost all impact conditions. Only one repeat is shown in figure 7 for the sake of clarity. The subfigures are ordered by increasing values of Γ. Note that some 50 Hz oscillations due to electric noise are visible in figures 7b and 7e. This issue was fixed during the campaign, but some of the measurements are polluted.

It appears from figure 7 that, depending on the values of Γ and δ, some force measurements are impulsive and others are not. For instance, in figure 7g, the force time history for $\bar{\delta} = 0.043$ is impulsive while the one for $\bar{\delta} = 0.003$ is not.

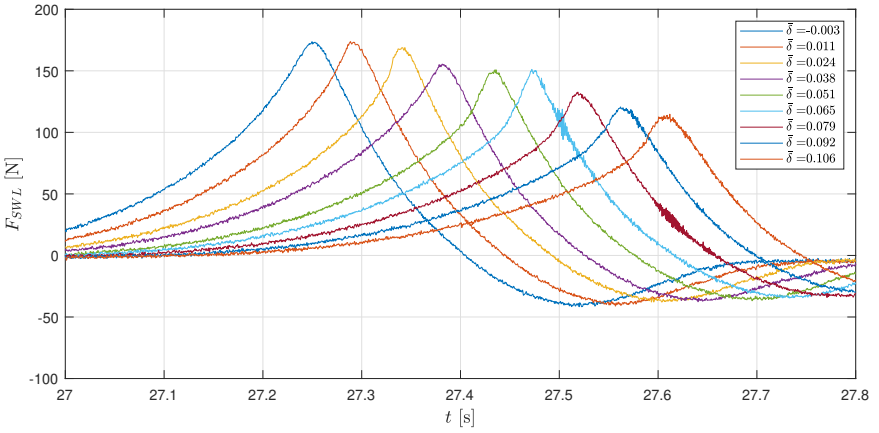

(a) Wave 2: $\Gamma = 0.8$, $T_p = 2.25$ s, $H_s = 0.13$ m

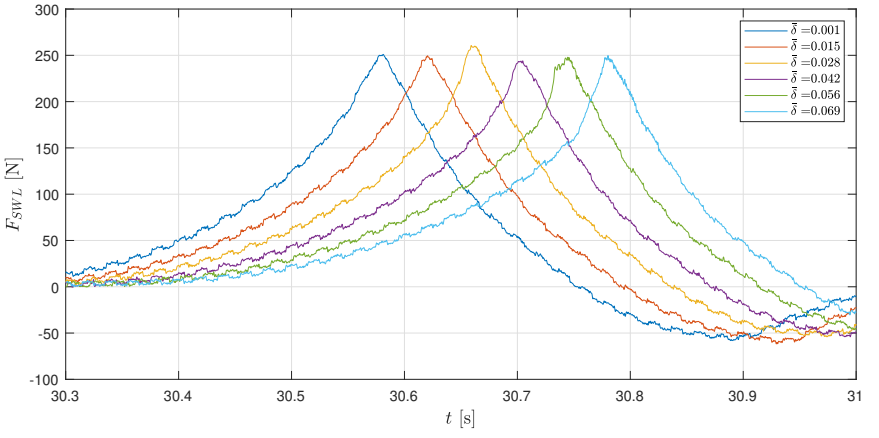

(b) Wave 1: $\Gamma = 0.97$, $T_p = 2.25$ s, $H_s = 0.12$ m

Figure 7: Evolution of the time-histories of the force with the non-dimensional distance to breaking $\bar{\delta}$ for the different waves

However, for some conditions, it is not easy to assess whether the force is impulsive or not. For example, it is not clear if the force time history corresponding to $\bar{\delta} = 0.016$ in figure 7g should be considered as impulsive or not. Even if the presence of a dynamic response is linked to the impulsive nature of the force, this response is structure dependent; thus, it is not reliable to discriminate the impulsive nature of the excitation force based on the response of the structure.

For the waves with the smallest values of Γ, namely waves 2 ($\Gamma = 0.8$) and 1 ($\Gamma = 0.97$), there is no value of $\bar{\delta}$ for which an impulsive increase of the measured force is observed (see figures 7a and 7b). For wave 2, the magnitude of the impact force slightly decreases when $\bar{\delta}$ increases, while it is rather constant for wave 1. For the other wave cases, corresponding to values of Γ greater than one, some values of $\bar{\delta}$ lead to an impulsive force increase while others do not. Small values of $\bar{\delta}$, i.e. close to zero, either present a small impulsive increase or are non-impulsive. Up to a value of $\bar{\delta}$ of about 0.05, the magnitude of the impact force F_{SWL} increases with $\bar{\delta}$. The highest magnitude of F_{SWL} is reached for values of $\bar{\delta}$ in the interval

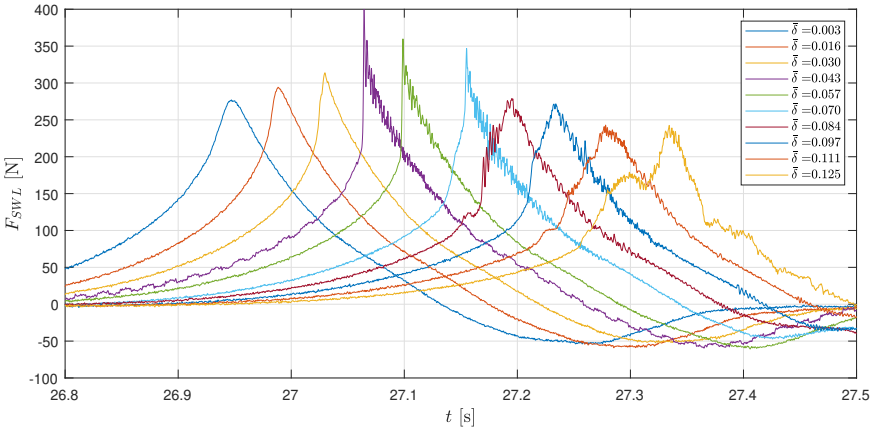

(c) Wave 23: $\Gamma = 1.29$, $T_p = 2.25$ s, $H_s = 0.135$ m

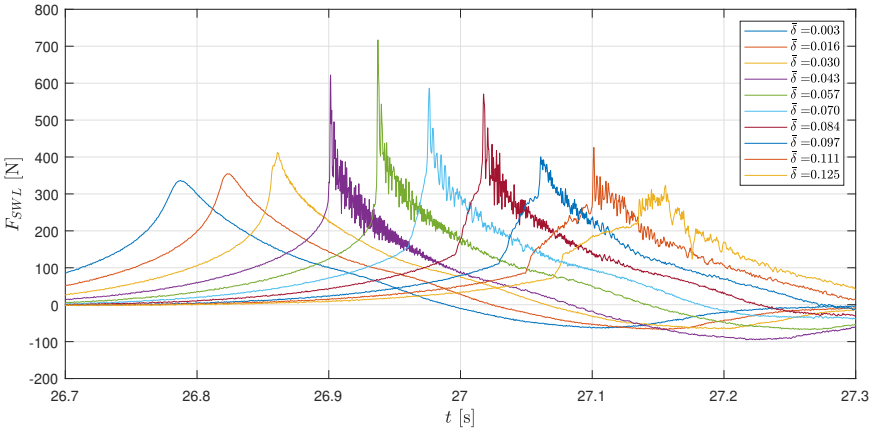

(d) Wave 24: $\Gamma = 1.82$, $T_p = 2.25$ s, $H_s = 0.14$ m

Figure 7: Evolution of the time-histories of the force with the non-dimensional distance to breaking $\bar{\delta}$ for the different waves

[0.04; 0.06]. The impacts for which $\bar{\delta}$ is in this interval are the ones showing the highest peak forces and the shortest rising times. For larger values of $\bar{\delta}$, the magnitude of F_{SWL} slowly decreases. It will be shown in the following sections that the wave impacts with values of $\bar{\delta}$ higher than 0.06 correspond to the impact of significantly overturned waves for which a jet is formed.

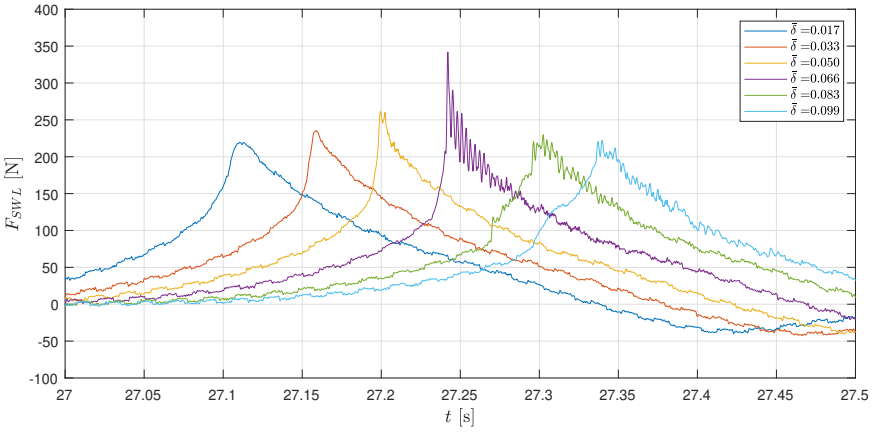

(e) Wave 15: $\Gamma = 1.83$, $T_p = 2.0$ s, $H_s = 0.10$ m

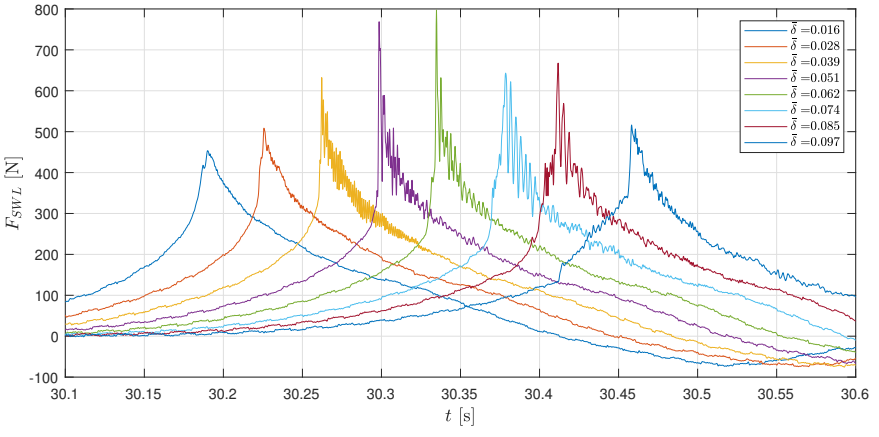

(f) Wave 7: $\Gamma = 1.93$, $T_p = 2.49$ s, $H_s = 0.13$ m

Figure 7: Evolution of the time-histories of the force with the non-dimensional distance to breaking $\bar{\delta}$ for the different waves

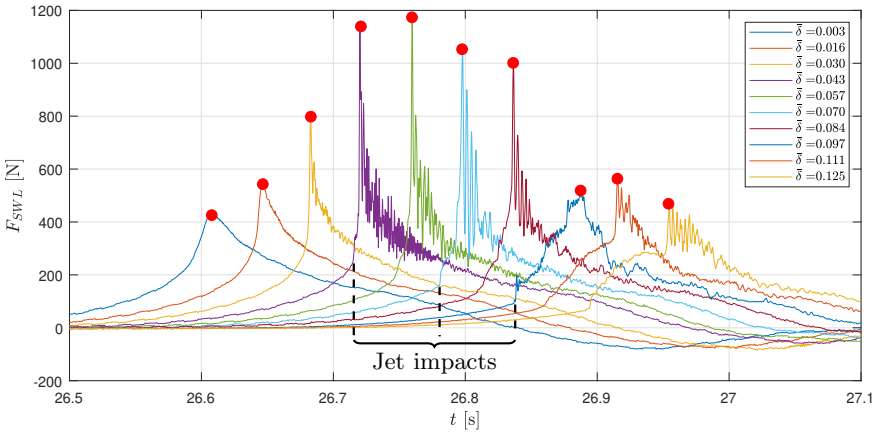

(g) Wave 3: $\Gamma = 3.01$, $T_p = 2.25$ s, $H_s = 0.15$ m. The dashed vertical lines are placed at the instants at which the forces first increase due to the impact of the jet. The red dots correspond to the magnitudes of the impact forces.

Figure 7: Evolution of the time-histories of the force with the non-dimensional distance to breaking $\bar{\delta}$ for the different waves

4.3. *Shape of the wave at impact for different distances to breaking*

It appeared in the previous section that different distances to breaking, i.e. different wave shapes at impact, may lead to very different force time histories. This section is devoted to the influence of the wave shape at impact on the characteristics of the force time history. The shape of wave 3 at the instant of maximum force for different distances to breaking is illustrated in figure 8 with high-speed video camera images. These instants are indicated by the red dots shown in figure 7g. The wave profiles obtained with the FNPF solver at the same instant are shown for comparison. The solid vertical line superimposed to the numerical profile indicates the position of the front face of the cylinder. For values of $\bar{\delta}$ higher than 0.084, the numerical free-surface profiles are not shown because they are not available at the instant of maximum force (the FNPF simulations stop when the tongue of the crest touches the water bulk). Note that the numerical free-surface profiles depicted in figure 7g were time shifted of 20 ms. As discussed in Hulin (2024), this time shift allowed to compensate for the delay between the experimental and numerical wave profiles. The images depicted in figure 7g show that for $\bar{\delta}$ values higher than 0.043 (figures 8d and below), the tongue of the wave has already reached the cylinder at the instant of maximum force. This is confirmed by the numerical free-surface profiles. It is likely that the impact of the tongue on the cylinder is responsible for the rather rapid but smaller force increases prior to the main impulse visible on the force time-histories of the impact of wave 3 depicted in figure 7g. These increases occur for $\bar{\delta} = 0.043$ and higher values. The black vertical dashed lines indicate the time instants at which these first force increases are observed. The fact that two different impacts (of the wave tongue and vertical front) occur when the wave crest has overturned is also supported by the studies of Zhou *et al.* (1991); Chan *et al.* (1995); Manjula *et al.* (2013); Govindasamy *et al.* (2023), who reported the appearance of two pressure peaks for wave impacts with high values of $\bar{\delta}$.

It also appears in figure 8 that at the instant of maximum force, the locally vertical part of the wave, which position is indicated by the dashed vertical line, is still far from the front face of the cylinder. In the basin, the wave profile is modified by the presence of the cylinder. It is likely that this modification is such that at the instant of maximum force, the locally vertical front indeed reaches the front face of the cylinder in the basin.

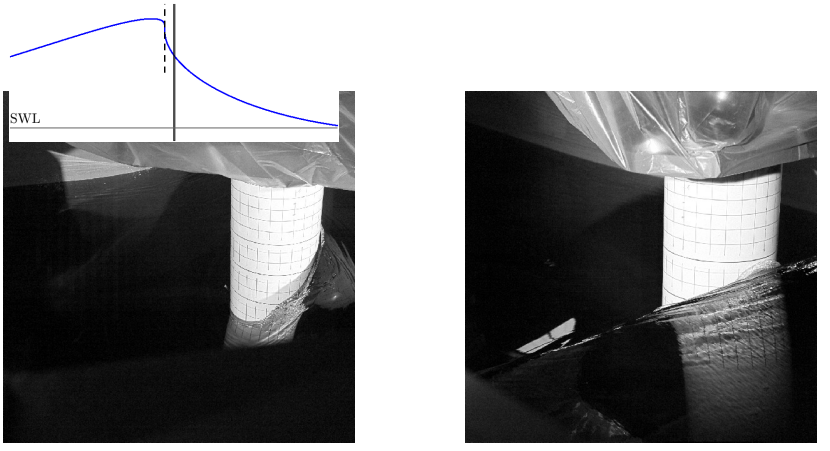

(a) $\bar{\delta} = 0.003$

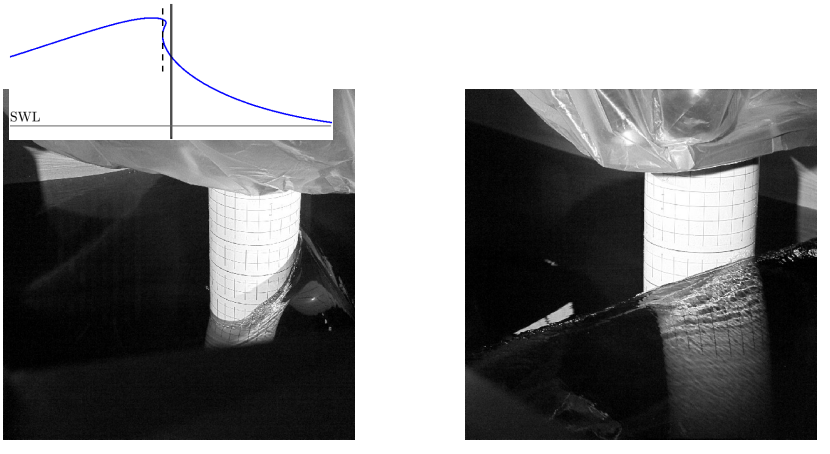

(b) $\bar{\delta} = 0.016$

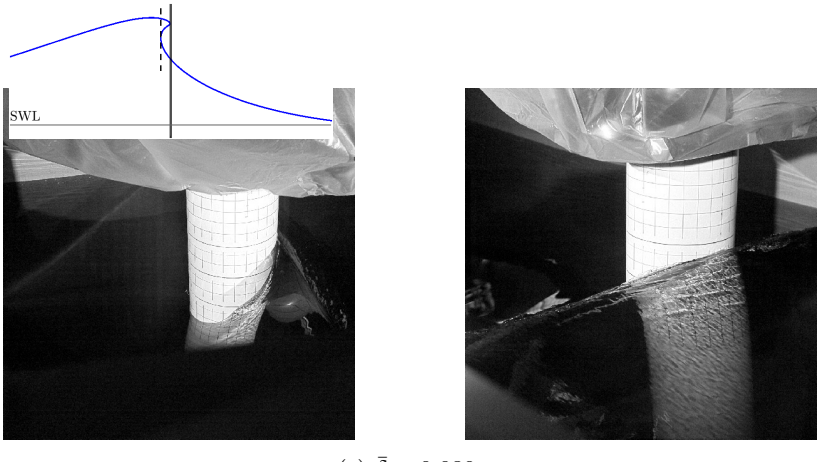

(c) $\bar{\delta} = 0.030$

Figure 8: Images of wave 3 impacting the mockup for various values of $\bar{\delta}$. All the images are taken at the instant at which the impact load is maximum. The plot in the upper left corner corresponds to the numerical free-surface profile at the same instant. The solid vertical line indicates the position of the front face of the cylinder. The dashed vertical line indicates the position of the locally vertical front.

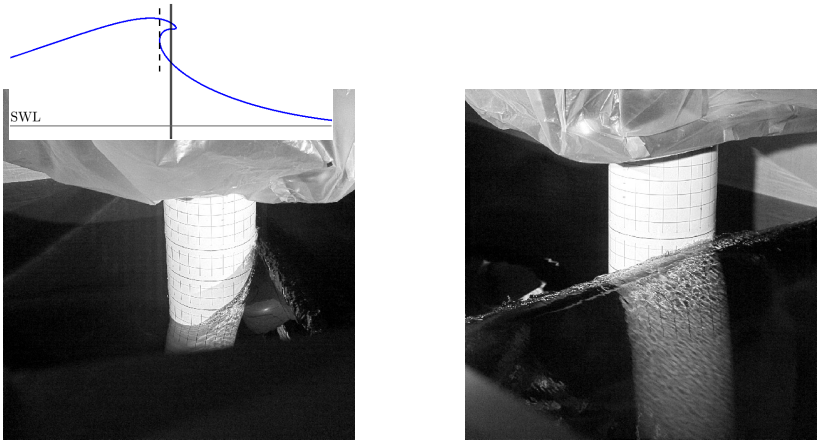

(d) $\bar{\delta} = 0.043$

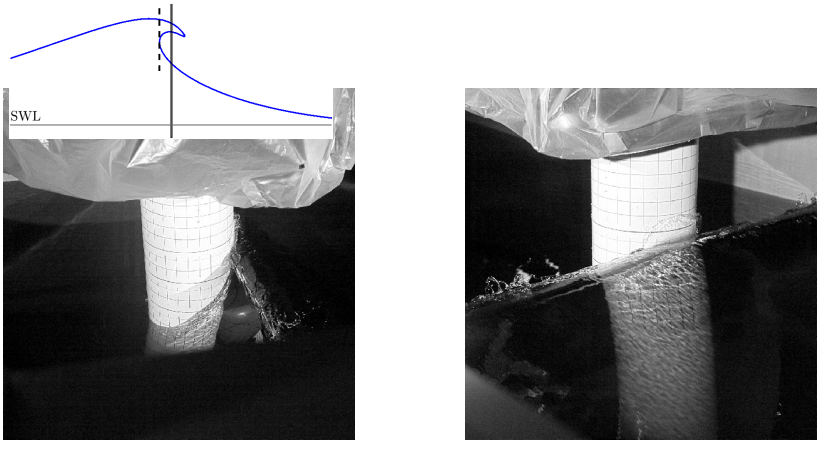

(e) $\bar{\delta} = 0.057$

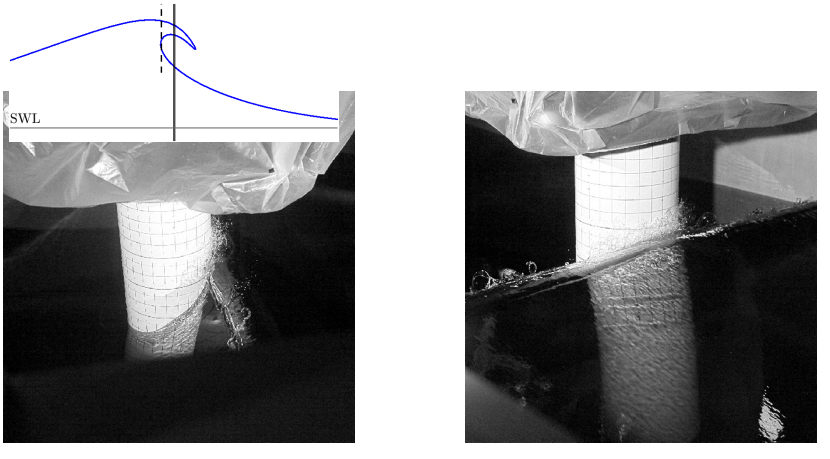

(f) $\bar{\delta} = 0.070$

Figure 8: Images of wave 3 impacting the mockup for various values of $\bar{\delta}$. All the images are taken at the instant at which the impact load is maximum. The plot in the upper left corner corresponds to the numerical free-surface profile at the same instant. The solid vertical line indicates the position of the front face of the cylinder. The dashed vertical line indicates the position of the locally vertical front.

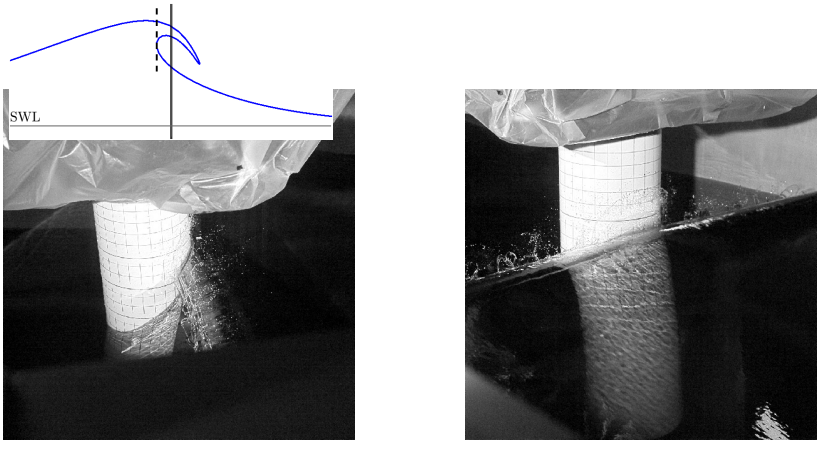

(g) $\bar{\delta} = 0.084$

(h) $\bar{\delta} = 0.097$

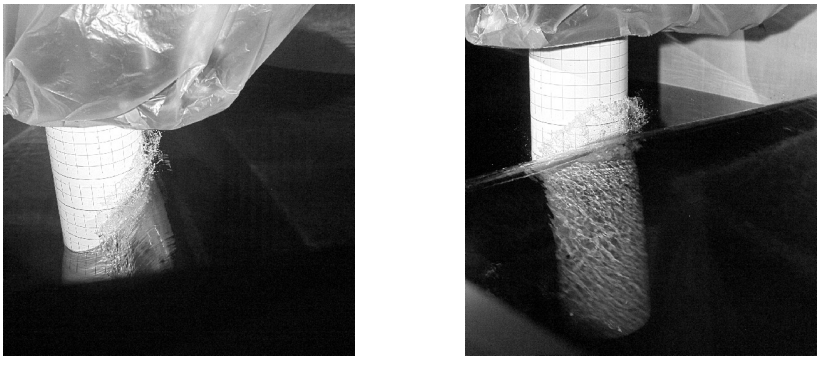

(i) $\bar{\delta} = 0.111$

Figure 8: Images of wave 3 impacting the mockup for various values of $\bar{\delta}$. All the images are taken at the instant at which the impact load is maximum. The plot in the upper left corner corresponds to the numerical free-surface profile at the same instant. The solid vertical line indicates the position of the front face of the cylinder. The dashed vertical line indicates the position of the locally vertical front.

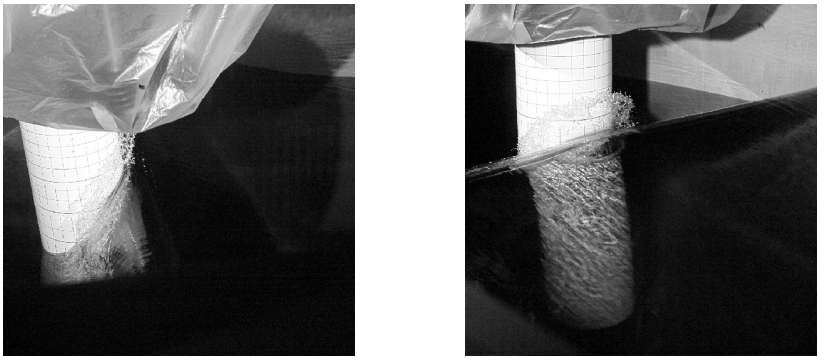

(j) $\bar{\delta} = 0.125$

Figure 8: Images of wave 3 impacting the mockup for various values of $\bar{\delta}$. All the images are taken at the instant at which the impact load is maximum. The plot in the upper left corner corresponds to the numerical free-surface profile at the same instant. The solid vertical line indicates the position of the front face of the cylinder. The dashed vertical line indicates the position of the locally vertical front.

4.4. *Influence of wave diffraction on the force time histories*

In section 4.2, we observed that impact conditions with small values of Γ or values of $\bar{\delta}$ close to zero do not lead to an impulsive force increase although the profile of the undisturbed wave presents a vertical front when it reaches the location of the cylinder. It is likely that this phenomenon is due to the fact that the shape of the wave is affected by the presence of the cylinder prior to the impact. This modification of the wave profile in the vicinity of the cylinder can indeed be observed on the high-speed video camera images. For the cases that do not show an impulsive increase of the force, we observe the appearance of a run-up that prevents the vertical front of the wave from impacting the cylinder. This is illustrated in figure 9 which presents images taken during two impacts of wave 24 with different values of $\bar{\delta}$. The images on the left correspond to $\bar{\delta} = 0.016$ and the images on the right to $\bar{\delta} = 0.043$. It can be seen in figure 7d that $\bar{\delta} = 0.016$ does not lead to an impulsive force increase while $\bar{\delta} = 0.043$ does. In figure 9, the images in the first raw (figure 9a) were taken 10 ms before the measured force reaches its maximum value, the images in the second raw (figure 9b) at the instant t_{max} (when the force is maximum) and the images in the third raw (figure 9c) 10 ms after t_{max}. The run-up is already visible 10 ms before the maximum force is reached for the non-impulsive case $\bar{\delta} = 0.016$ (see the blue arrow in figure 9a) while it is not for the impulsive case $\bar{\delta} = 0.043$. At the instant of maximum force (figure 9b), the extent of the run-up has increased for the case $\bar{\delta} = 0.016$ while the wetted surface expansion is not yet visible for the case $\bar{\delta} = 0.043$. The extent of the cylinder surface affected by the run-up is strongly increased 10 ms after the instant of maximum force (figure 9c) for the non-impulsive case while the fragmentation of the jet visible on the right of figure 9c indicates that a hydrodynamic impact occurred.

These images show that the presence of the structure may modify the wave in such a way that hydrodynamic impact is hindered. For waves 1 and 2, which correspond to low values of Γ and for which no value of $\bar{\delta}$ leads to an impulsive force increase, a similar run-up was observed. One may also expect that in certain

cases for which a wave impact occurs, the force evolution may be affected by wave diffraction effects. This assumption is supported by the results of Batlle Martin *et al.* (2023) who observed through numerical simulations that the vertical part of a wave that may induce impact is reduced when the diameter of the cylinder is increased. The importance of the wave diffraction was also highlighted by Chan & Melville (1989) who measured the impact forces induced by breaking waves impacting on a vertical circular cylinder and a vertical wall. They observed that a vertical wall, which corresponds to the case of a cylinder with an infinite diameter, has a greater influence on the development of the breaking wave than a cylinder. In the present experiments, the radius of the cylinder was kept constant, but waves of different sizes were investigated. More precisely, the ratio R/L between the radius of the cylinder and the characteristic wavelength of the impacting wave is ranging from 2.3×10^{-2} to 3.3×10^{-2}, with 5 out of 7 waves corresponding to $R/L = 2.7 \times 10^{-2}$. These values were chosen so as to be representative of the wave conditions that may be experienced by a SPAR-type wind turbine floater. Given the rather limited range of values, it has not been possible to characterise the influence of the R/L ratio on the perturbation of the wave front and on the resulting impact force. As a consequence, one should keep in mind that the non-dimensional force measurements presented in the following sections may not be valid for impact conditions where the ratio R/L is significantly different from the ones used in the present study.

5. Influence of the impact conditions on the magnitude of the impact force

5.1. *Evolution of the magnitude of the impact force with the impact conditions*

In the present section, we investigate the influence of the impact conditions, i.e. of the values of $\bar{\delta}$ and Γ, on the magnitude of the impact force. As a reminder, the term "magnitude of the impact force" denotes the maximum value over time reached by the measured force F_{SWL}. For wave 3, the magnitude of the impact force obtained for different values of $\bar{\delta}$ is indicated by the red dots shown in figure 7g. The magnitude of the impact force obtained for each impact condition and each repeat is reported in figure 10. Each colour is associated to a particular wave. In accordance with the observations of section 4, for the smaller values of Γ ($\Gamma < 1$ for waves 1 and 2), the magnitude of the impact force is almost independent of the value of $\bar{\delta}$. For higher values of Γ, the maximum value of the impact force magnitude is reached close to $\bar{\delta} = 0.05$. For these 5 wave cases with $\Gamma > 1$, the increase of the force prior to the peak is steeper than the subsequent decrease. It is also interesting to note that waves 15, 7 and 24, whose values of Γ are around 1.9, present rather close evolutions for the magnitude of the non-dimensional impact force.

5.2. *Maximum impact force induced by a given wave*

As observed in the previous section, the magnitude of the impact force generated by a given wave depends on the distance to breaking δ. In the present section, the focus is on the maximum of the magnitude of the impact force that may be reached for a given wave and its evolution as a function of Γ.

For each impact condition, i.e. each couple $(\Gamma, \bar{\delta})$, we compute the mean value of the impact force magnitude, denoted by $\bar{F}_{SWL}^{mean}$, over the different repeats of

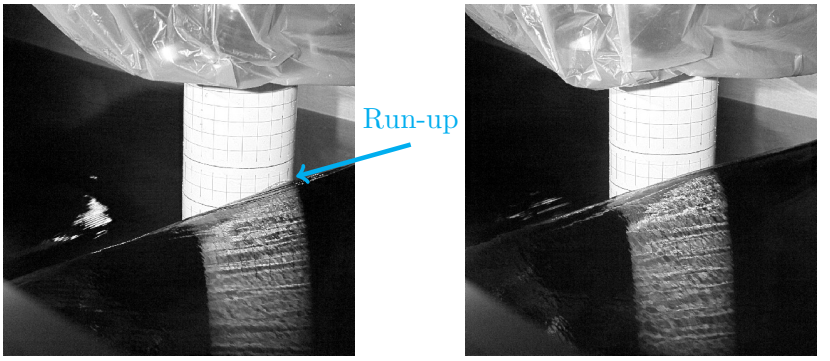

(a) $t_{max} - 10$ ms

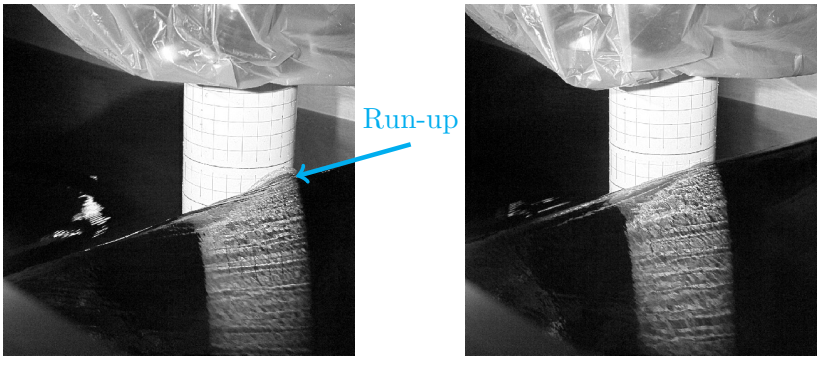

(b) t_{max}

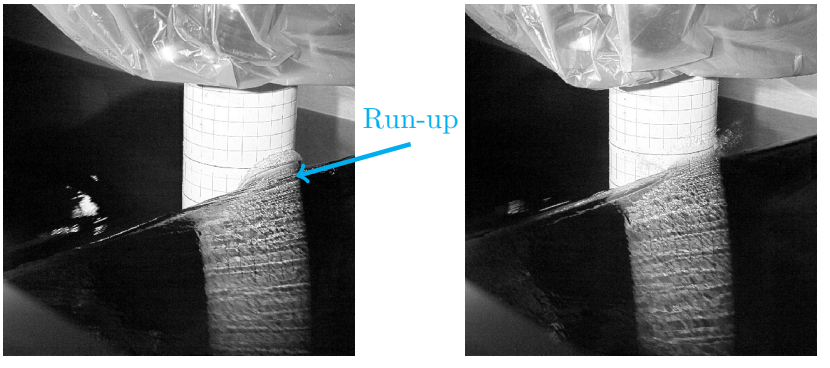

(c) $t_{max} + 10$ ms

Figure 9: Images of the impact of wave 24 on the vertical cylinder at different instants around the instant of the maximum force t_{max}. The pictures on the left correspond to $\bar{\delta} = 0.016$ while the pictures on the right correspond to $\bar{\delta} = 0.043$.

the experiment. The values of $\bar{F}_{SWL}^{mean}$ obtained for the different values of $\bar{\delta}$ for wave 3 ($\Gamma = 3.01$) are represented in figure 10 by red dots. It appears that there is a value of $\bar{\delta}$ for which $\bar{F}_{SWL}^{mean}$ is maximum. This maximum impact force, that is illustrated by the blue arrow in figure 10, is denoted by $\bar{F}_{SWL}^{max}$.

The evolution of $\bar{F}_{SWL}^{max}$ as a function of Γ is depicted in figure 11. Each circle corresponds to a wave case and the solid line is a linear approximation of the evolution of $\bar{F}_{SWL}^{max}$. The results presented in figure 11 show that the maximum non-dimensional impact force $\bar{F}_{SWL}^{max}$ is strongly correlated to the breaking strength

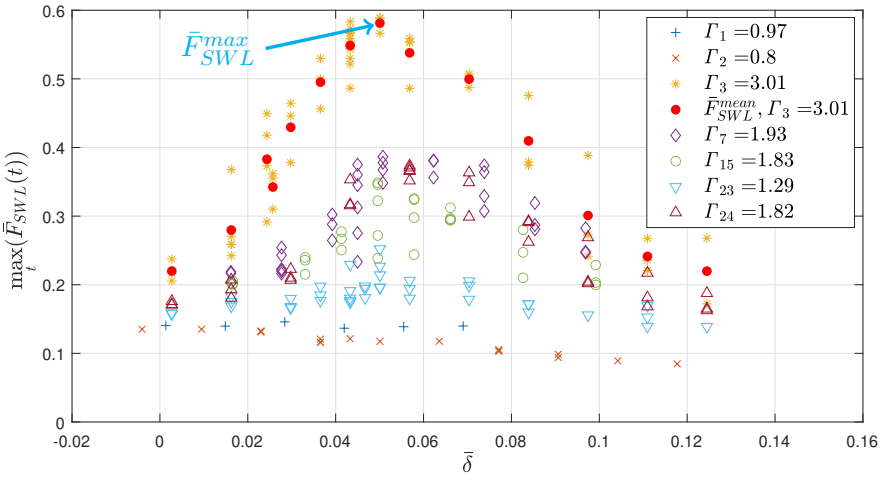

Figure 10: Evolution of the magnitude of the non-dimensional force $\bar{F}_{SWL}$ as a function of $\bar{\delta}$. In the legend, the Γ indices correspond to the wave numbers given in table 2. The red dots, shown only for wave 3, correspond to the mean value of the impact force magnitude over the different repeats of the same impact conditions.

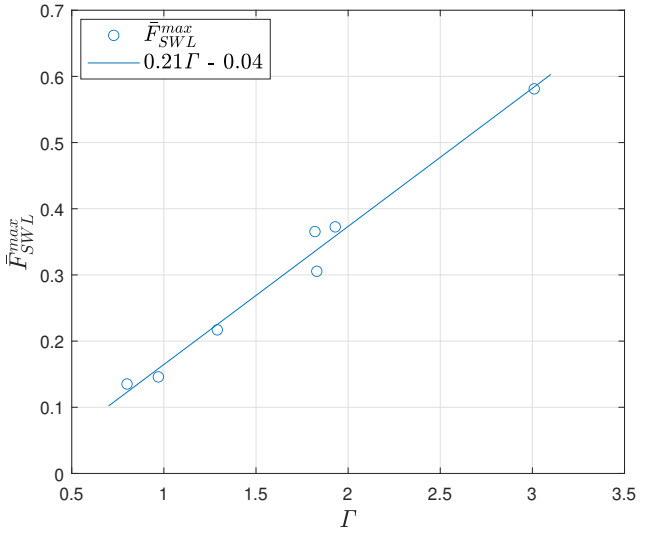

Figure 11: Evolution of the maximum impact force $\bar{F}_{SWL}^{max}$ as a function of Γ. Each circle corresponds to the maximum impact force obtained for a wave case. The solid line is a linear approximation of the evolution of $\bar{F}_{SWL}^{max}$ as a function of Γ.

Γ. This is an important outcome of the present study. Note also that the circles corresponding to waves 7, 15 and 24 lie close to each other in figure 11. These 3 waves have different wavelengths ranging from 6.05 m to 8.67 m and wave heights ranging from 0.30 m to 0.41 m, but they are all mild plunging breakers

with a value of Γ of approximately 1.8. The present results thus suggest that the obtained evolution of $\bar{F}_{SWL}^{max}$ is independent of the wave scale.

Note that the systematic variation of the values of δ that was carried out is of prime importance for the results presented in figure 11. Indeed, for wave 3 for instance, if $\bar{F}_{SWL}^{max}$ had been estimated at a δ value 20 cm smaller than the one leading to $\bar{F}_{SWL}^{max}$, the maximum force would have been underestimated by 30 %. In figure 7g, this would correspond to estimating $\bar{F}_{SWL}^{max}$ with the curve labelled $\bar{\delta} = 0.030$ instead of the curve labelled $\bar{\delta} = 0.057$. The value obtained for $\bar{F}_{SWL}^{max}$ would thus be close to the one obtained for wave 24. Studying the influence of the distance to breaking δ on the impact force appears as an important step in the determination of the maximum impact force $\bar{F}_{SWL}^{max}$ that may be induced by a breaking wave.

6. Identification of an empirical formula for the maximum impact force

This section is devoted to the development of an empirical formula for the maximum impact force induced by a breaking wave on a vertical cylinder. For each wave, we propose in section 6.1 an asymmetric Gaussian fit that describes the evolution of the maximum impact force as a function of $\bar{\delta}$. This fit depends on five parameters. Based on these parameters, we propose in section 6.2 an empirical formula that describes the evolution of the impact force as a function of $\bar{\delta}$ and Γ.

6.1. *Parametrisation of the maximum impact force as a function of* $\bar{\delta}$

Considering the evolution of the non-dimensional force $\bar{F}_{SWL}$ as a function of $\bar{\delta}$ that was described in section 5.1, we propose to fit the force evolution for each wave using two Gaussian functions. One function describes the increase of the magnitude of the force prior to its peak and the other one describes the subsequent decrease. Using two functions allows to account for the fact that the increase of the force magnitude is faster than its subsequent decrease. In addition, a constant $\bar{F}_0$ is added to the fit to account for the fact that the force magnitude does not seem to tend to zero for negative and high values of $\bar{\delta}$. For waves 1 and 2, for which the magnitude of the force is almost independent of $\bar{\delta}$, we only identify this constant parameter. Consequently, for waves 1 and 2, this constant corresponds to the mean value of the magnitude of the impact force obtained for the different impact conditions. For the other waves, the parametric function writes:

$$f(\bar{\delta}) = \bar{F}_0 + \bar{F}_G \exp\left(-\frac{1}{2}\frac{(\bar{\delta}-\bar{\delta}_{max})^2}{\sigma^2}\right), \text{ with } \begin{cases} \sigma = \sigma_l & \text{if } \bar{\delta} < \bar{\delta}_{max} \\ \sigma = \sigma_r & \text{if } \bar{\delta} > \bar{\delta}_{max} \end{cases}. \quad (6.1)$$

This function depends on 5 parameters, which can be interpreted as follows. Parameter $\bar{F}_0$ corresponds to the non-impulsive part of the force. As explained previously, we assume that this parameter does not depend on $\bar{\delta}$. In other words, it is assumed that the variation of the non-impulsive part of the force with the distance to breaking is negligible compared to the variation of the impulsive part. Parameter $\bar{\delta}_{max}$ is the value of $\bar{\delta}$ for which the fit reaches its maximum, i.e. the value of $\bar{\delta}$ for which the most severe impact is obtained. Therefore, the maximum value of the impact force magnitude corresponds to $\bar{F}_{SWL}|_{\bar{\delta}_{max}} = \bar{F}_0 + \bar{F}_G$. The force $\bar{F}_G$ can thus be identified as the impulsive part of $\bar{F}_{SWL}|_{\bar{\delta}_{max}}$. Parameters

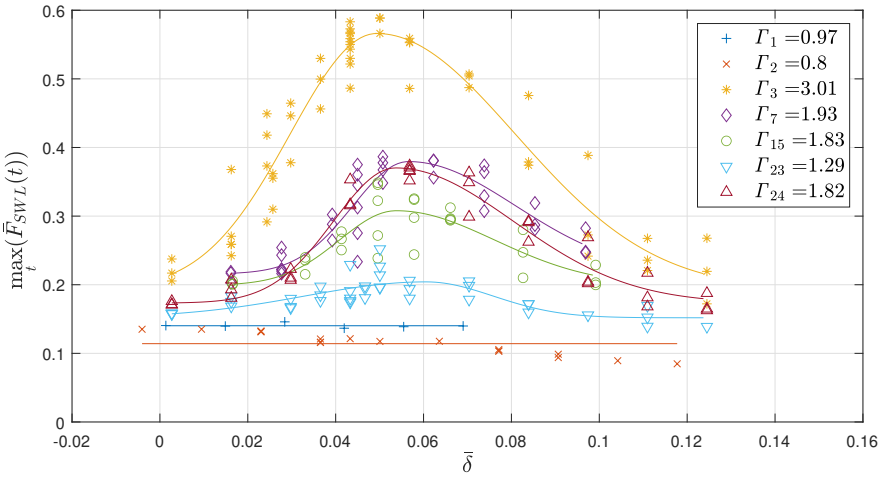

Figure 12: Evolution of the magnitude of the non-dimensional impact force as a function of $\bar{\delta}$. The wave numbers correspond to the index of Γ. For each wave, the solid line corresponds to the result of the fit obtained with the parametric function of equation 6.1.

σ_l^2 and σ_r^2 characterise the range of $\bar{\delta}$ values over which a hydrodynamic impact may occur for values of $\bar{\delta}$ smaller or higher than $\bar{\delta}_{max}$, respectively.

The obtained fits of the force evolutions are depicted in figure 12, along with the experimental measurements. The values obtained for the parameters of the fits are given in table 3 (appendix A) for the 7 wave cases. For waves 3, 7, 15 and 24, figure 12 shows that the fits are in close agreement with the measured force evolution. For wave 23 ($\Gamma = 1.29$), the value of $\bar{\delta}$ for which the fit is maximum does not correspond to the value of $\bar{\delta}$ for which $\bar{F}_{SWL}^{max}$ is reached. Also, the fit presents a force increase that is less pronounced than the subsequent decrease. We think that this difference could be due to the fact that the non-impulsive part of the force is higher than its impulsive part. Indeed, for wave 23, $\bar{F}_G$ is smaller than $\bar{F}_0$ (this is not the case for waves 3, 7, 15 and 24). Small variations of the non-impulsive part of the force, as the ones observed for wave 2, may thus influence the fit that is assumed to account for the impulsive part of the force. As a consequence, the fit may not be well-suited for the impact of weak breaking waves. For this reason, the parameters $\bar{\delta}_{max}$, σ_l and σ_r obtained for wave 23 will be discarded in the following section that investigates the evolution of the fit parameters as a function of Γ.

6.2. *Evolution of the parameters of the fit as a function of Γ*

The evolution of the impulsive and non-impulsive parts of the force, respectively $\bar{F}_G$ and $\bar{F}_0$, that were obtained for waves 3, 7, 15 and 24 are shown in figure 13 as a function of Γ. The solid lines correspond to linear interpolations of these two quantities and each marker corresponds to a wave case. It appears that the evolution of $\bar{F}_0$ is nearly independent of Γ. For the 4 considered wave cases, we obtain:

$$\bar{F}_0 \approx 0.20. \tag{6.2}$$

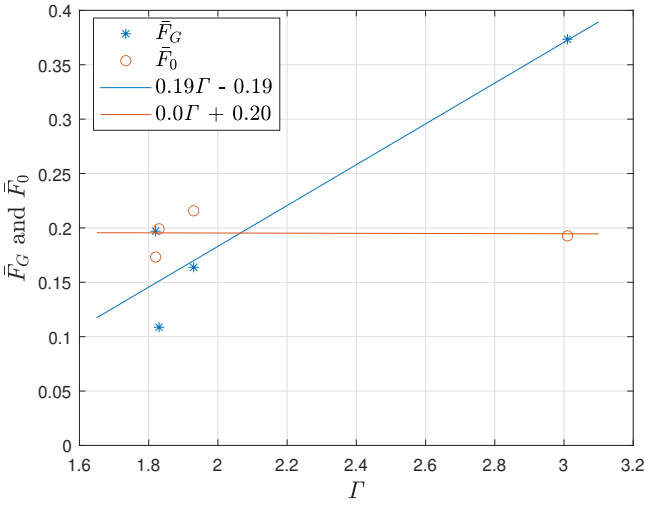

Figure 13: Evolution of parameters $\bar{F}_0$ and $\bar{F}_G$ as a function of Γ

A linear approximation of the evolution of the impulsive part of the force $\bar{F}_G$ as a function of Γ leads to:

$$\bar{F}_G \approx 0.19\Gamma - 0.19. \tag{6.3}$$

The assumption of a linear evolution of $\bar{F}_G$ with the Γ parameter is also supported by the results presented in section 5.2 (see figure 11). Indeed, when the maximum of the magnitude of the measured force $\bar{F}_{SWL}^{max}$ is considered, we observe a similar relationship with the Γ parameter for the seven wave cases.

For the wave cases 3, 7, 15 and 24, we obtain mean$(\bar{\delta}_{max}) = 0.053$, which means that δ_{max} corresponds to 5.3 % of the wavelength of the impacting wave. This is in close agreement with the value of 6 % of the wavelength obtained in the study by Sawaragi & Nochino (1984). To the best of the authors knowledge, the study by Sawaragi & Nochino (1984) is the only one giving an estimate of $\bar{\delta}_{max}$. Nevertheless, other studies (e.g., Ma *et al.* 2020; Zhang *et al.* 2024) observed that the strongest impact loads were obtained for the impact of an overturned wave, the tongue of which has not impinged the free surface yet. This is also in agreement with the value of $\bar{\delta}_{max}$ obtained in the present study. Indeed, an image of wave 3 for which $\bar{\delta} \approx \bar{\delta}_{max}$ is depicted in figure 8e at the instant of maximum force. It corresponds to a significantly overturned wave, the tongue of which has not impinged the free surface yet.

The evolution of the other parameters of the fit, namely σ_l and σ_r, is shown in figure 14. We observe that the values of σ_l and σ_r obtained for wave 3 are higher than the ones obtained for the other wave cases. This would mean that a wave with a high value of Γ may induce impact over a wider region than a wave with a smaller value of Γ. However, as the variations of σ_l and σ_r with Γ are rather limited, we propose to approximate σ_l and σ_r using their mean values, respectively mean$(\sigma_l) = 0.015$ and mean$(\sigma_r) = 0.026$. These mean values are represented by the two horizontal lines in figure 14.

Based on these results and the non-dimensionalisation of equation 2.2, we suggest that the dimensional impulsive part F_G of the force acting above the

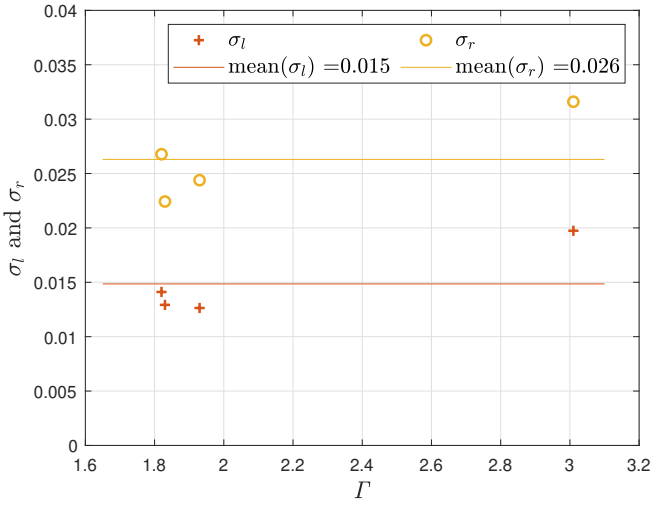

Figure 14: Parameters $\bar{\delta}_{max}$, σ_l and σ_r as a function of Γ for the wave cases listed in table 2.

SWL can be estimated as:

$$F_G = C_{WS}(\Gamma, \bar{\delta})\rho c^2 R \eta_b, \tag{6.4}$$

where C_{WS} is a wave slamming coefficient that depends on $\bar{\delta}$ and Γ. This wave slamming coefficient reads:

$$\begin{gathered} C_{WS}(\Gamma, \bar{\delta}) = \pi(a_\Gamma \Gamma + b_\Gamma) \exp\left(-\frac{1}{2}\frac{(\bar{\delta} - \bar{\delta}_{max})^2}{\sigma^2}\right), \\ \text{with} \begin{cases} \sigma = \sigma_l & \text{if } \bar{\delta} < \bar{\delta}_{max} \\ \sigma = \sigma_r & \text{if } \bar{\delta} > \bar{\delta}_{max} \end{cases}. \end{gathered} \tag{6.5}$$

The values of the different parameters given in the previous equation are:

$$\begin{aligned} a_\Gamma &= 0.19 \\ b_\Gamma &= -0.19 \\ \bar{\delta}_{max} &= 0.053 \\ \sigma_l &= 0.015 \\ \sigma_r &= 0.026. \end{aligned} \tag{6.6}$$

This formula was obtained from values of Γ ranging from 1.8 to 3. Validating this formula outside of this range would require additional investigations.

7. Conclusions

We quantitatively investigated the influence of the distance to breaking and of the breaking strength on the force generated by a breaking wave impacting a segmented vertical cylinder. The strength of the breaking wave was characterised by the Γ parameter introduced by Derakhti *et al.* (2018). The distance to breaking was computed as the distance between the front face of the cylinder and the

breaking location. Our analysis is based on the force measured above the still water level. Seven different wave cases displaying various breaking strengths Γ were investigated. The distance δ was systematically varied for the seven wave cases. The values of the parameters δ and Γ were estimated using a fully non-linear potential flow solver. The compensation methodology proposed in Tassin *et al.* (2024) was used to reduce the amplitude of the force oscillations induced by the dynamic structural response of the mockup.

For each wave case, the time-histories of the impact forces obtained for different values of δ are presented. It appears that for values of Γ lower than one, no position of the mockup leads to an impulsive force. The first wave case inducing a hydrodynamic impact corresponds to a value of $\Gamma = 1.29$. For higher values of Γ, the higher the value of Γ, the stronger the impact force. Thanks to the high-speed video camera images, we highlighted that the absence of hydrodynamic impact for some wave cases and some values of δ is a consequence of the presence of a run-up that hinders the impact of the wave front on the cylinder. We observed that the maximum value of the impact force magnitude is linearly related to the Γ parameter. The evolution of the magnitude of the impact force with the non-dimensional distance to breaking $\bar{\delta}$ is as follows: it increases until it reaches a peak value for $\bar{\delta} \approx 0.05$; then, a slower decrease is observed.

From the experimental force measurements, we fitted the evolution of the magnitude of the force with the distance $\bar{\delta}$ for each wave using an asymmetric Gaussian function. For all the wave cases inducing large impulsive loads, we observed that the sole parameter of the fit that depends on Γ is the maximum value of the impact force magnitude. The other parameters such as the position of the maximum, $\bar{\delta}_{max}$, and the right and left width of the Gaussian functions are nearly constant. Based on these results, we proposed an empirical formula to predict the magnitude of the impulsive part of the force as a function of $\bar{\delta}$ and Γ.

The conclusions of this work are based on a compilation of more than 180 impact experiments. Nevertheless, several limitations of the present study were identified and could be improved in future works. First, only seven breaking wave cases were exploited, out of which two did not induce hydrodynamic impact. This limitation is related to the important experimental time required to vary the distance to breaking δ for each wave case. Moreover, it is necessary to wait for 45 minutes between two consecutive tests to ensure that the flume is at rest. This ensures a good repeatability of the measurements ($\approx$ 5 % variations on the magnitude of the force), but it is at the expense of the number of impact conditions that could be investigated. This reduced number of waves is not sufficient to investigate the influence of the scale of the wave on the impact force. As mentioned in section 4.4, we observed that the run-up influences the presence of hydrodynamic impact. It is thus likely that it also influences the magnitude of the impact force. This has indeed been shown numerically by Batlle Martin *et al.* (2023). The importance of the run-up is likely driven by the ratio between the wavelength of the impacting wave and the radius of the cylinder. As such, it would be of interest to extend the present study to breaking waves of different sizes or to cylinders of different sizes. Another difficulty that was encountered during the study is the computation of the Γ parameter. Indeed, we had to rely on numerical simulations to estimate the value of Γ for the different wave cases. Ideally, this quantity should be estimated experimentally, but this would require significant developments without guaranties of success. Indeed, the computation of Γ from numerical results is already delicate (see Hulin *et al.* 2025), so computing Γ from

experimental results is expected to be even more difficult because of inherent measurement uncertainties (such as signal noise).

Acknowledgements. Florian Hulin gratefully acknowledges the support of Stephan Grilli that furnished the FNPF solver used to model the breaking waves. Florian Hulin and Alan Tassin are grateful to Matthieu Laurent from Ifremer for his contribution to the design of the segmented model, and to the technical team of Ifremer for their support during the experimental campaign.

Funding. This work is performed under financial support of grant ANR10IEED-0006-34, France Energies Marines project DIMPACT (Dimensionnement d'éoliennes flottantes prenant en compte les impacts de la raideur et du déferlement des vagues).

Declaration of interests. The authors report no conflict of interest.

Data availability statement. The data that support the findings of this study are openly available in [repository name] at http://doi.org/[doi], reference number [reference number]. See JFM's research transparency policy for more information

Author ORCIDs. F. Hulin, https://orcid.org/0000-0002-5759-4706; A. Tassin, https://orcid.org/0000-0002-7641-6147; N. Jacques, https://orcid.org/0000-0002-4146-3613, J.F. Filipot; https://orcid.org/0000-0003-0875-8791

Author contributions. Authors may include details of the contributions made by each author to the manuscript'

Appendix A. Parameters of the Gaussian fits

The parameters of the Gaussian fits presented in section 6.1 are given in table 3 along with the values of the Γ parameter of the breaking waves.

REFERENCES

Alsalah, Ali, Holloway, Damien, Mousavi, Mohsen & Lavroff, Jason 2021 Identification of wave impacts and separation of responses using EMD. *Mechanical Systems and Signal Processing* **151**, 107385.

Antonini, Alessandro, William Brownjohn, James Mark, Dassanayake, Darshana, Raby, Alison, Bassit, James, Pappas, Athanasios & D'Ayala, Dina 2021 A Bayesian inverse dynamic approach for impulsive wave loading reconstruction: Theory, laboratory and field application. *Coastal Engineering* **168**, 103920.

Batlle Martin, Marc, Harris, Jeffrey C., Filipot, Jean-François, Hulin, Florian, Tassin, Alan & Renaud, Paul 2023 Deep water focused breaking wave loads on a fixed cylinder. *Coastal Engineering* **186**, 104397.

Chan, Eng-Soon, Cheong, Hin-Fatt & Tan, Boon-Cheng 1995 Laboratory study of plunging wave impacts on vertical cylinders. *Coastal Engineering* **25** (1-2), 87–107.

Chan, E.-S. & Melville, W. K. 1989 Plunging Wave Forces on Surface-Piercing Structures. *Journal of Offshore Mechanics and Arctic Engineering* **111** (2), 92–100.

Derakhti, Morteza, Banner, Michael L. & Kirby, James T. 2018 Predicting the breaking strength of gravity water waves in deep and intermediate depth. *Journal of Fluid Mechanics* **848**, R2.

Ghadirian, Amin, Pierella, Fabio & Bredmose, Henrik 2023 Calculation of slamming wave loads on monopiles using fully nonlinear kinematics and a pressure impulse model. *Coastal Engineering* **179**, 104219.

Goda, Yoshimi, Haranake, Suketo & Kitahata, Masaki 1966 Study of impulsive breaking wave forces on piles. *Tech. Rep.*.

Govindasamy, Vijaya Kumar, Chella, Mayilvahanan Alagan, Sannasi Annamalaisamy, Sannasiraj & Rajamanickam, Panneer Selvam 2023 Impact pressure distribution and characteristics of breaking wave impact on a monopile. *Ocean Engineering* **271**, 113771.

Wave number	Γ	$\bar{F}_G$	$\bar{F}_0$	$\bar{\bar{\delta}}_{\max}$	σ_l	σ_r
1	0.97	0	0.14	0	0	0
2	0.8	0	0.114	0	0	0
3	3.01	0.37	0.19	0.049	0.020	0.032
7	1.93	0.16	0.22	0.057	0.013	0.024
15	1.83	0.11	0.20	0.054	0.013	0.022
23	1.29	0.05	0.15	0.061	0.028	0.015
24	1.82	0.20	0.17	0.054	0.014	0.027

Table 3: Parameters of the Gaussian fits for the different waves.

Grilli, S. T., Skourup, J. & Svendsen, I.A. 1989 An efficient boundary element method for nonlinear water waves. *Engineering Analysis with Boundary Elements* **6** (2), 97–107.

Grilli, S. T. & Subramanya, R. 1996 Numerical modeling of wave breaking induced by fixed or moving boundaries. *Computational Mechanics* **17** (6), 374–391.

Guo, Yinghao, Xiao, Longfei, Teng, Xiaoqing, Kou, Yufeng & Liu, Jiancheng 2020 Processing method and governing parameters for horizontal wave impact loads on a semi-submersible. *Marine Structures* **69**, 102673.

Ha, Yoon-Jin, Kim, Kyong-Hwan, Nam, Bo Woo & Hong, Sa Young 2020 Experimental investigation for characteristics of wave impact loads on a vertical cylinder in breaking waves. *Ocean Engineering* **209**, 107470.

Hulin, Florian 2024 Experimental study of the hydrodynamic loads generated by breaking wave impacts on floating offshore wind turbines. PhD Thesis, ENSTA Bretagne.

Hulin, Florian, Prevosto, Marc, Tassin, Alan, Filipot, Jean-françois, Jacques, Nicolas & Grilli, Stephan 2025 Breaking onset and breaking strength of focused wave packets: Linear prediction model and nonlinear numerical simulations. *Coastal Engineering* **197**, 104660.

von Karman, T. H. 1929 The impact on seaplane floats during landing. *Tech. Rep.* Technical note number 321.

Kjeldsen, Søren Peter, Tørum, Alf & Dean, Robert G. 1986 Wave Forces on Vertical Piles Caused by 2- and 3-Dimensional Breaking Waves pp. 1929–1942.

Ma, Yuxiang, Tai, Bing, Dong, Guohai & Perlin, Marc 2020 Experimental study of plunging solitary waves impacting a vertical slender cylinder. *Ocean Engineering* **202**, 107191.

Manjula, R., Sannasiraj, S. A. & Palanichamy, K. 2013 Laboratory Measurements of Breaking Wave Impact Pressures on a Slender Cylindrical Member. *The International Journal of Ocean and Climate Systems* **4** (3), 151–169.

Moalemi, Arefhossein, Bredmose, Henrik, Kristiansen, Trygve & Pierella, Fabio 2024 Wave front perturbation effect on the variability of monopile wave impact loads. *Journal of Fluid Mechanics* **984**, A65.

Paulsen, Bo Terp, Bredmose, Henrik & Bingham, Harry B. 2014 An efficient domain decomposition strategy for wave loads on surface piercing circular cylinders. *Coastal Engineering* **86**, 57–76.

Paulsen, Bo Terp, Sonneville, Ben de, Meulen, Michiel van der & Jacobsen, Niels Gjøl 2019 Probability of wave slamming and the magnitude of slamming loads on offshore wind turbine foundations. *Coastal Engineering* **143**, 76–95.

Rapp, R. J. & Melville, W. K. 1990 Laboratory measurements of deep-water breaking waves. *Philosophical Transactions of the Royal Society of London. Series A, Mathematical and Physical Sciences* **331** (1622), 735–800, publisher: Royal Society.

Renaud, P., Martin, M.B., Hulin, F., Harris, J., Filipot, J. F. & Scolan, Y. M.

2023 Semi-analytical load models describing the progressive immersion of a fixed vertical cylinder in a breaking wave. *Ocean Engineering* **276**, 114116.

Sawaragi, Toru & Nochino, Masao 1984 Impact Forces of Nearly Breaking Waves on a Vertical Circular Cylinder. *Coastal Engineering in Japan* **27** (1), 249–263.

Suja-Thauvin, Loup, Krokstad, Jørgen R, Bachynski, Erin E & de Ridder, Erik-Jan 2017 Experimental results of a multimode monopile offshore wind turbine support structure subjected to steep and breaking irregular waves. *Ocean Engineering* **146**, 339–351.

Tai, Bing, Ma, Yuxiang, Dong, Guohai, Koh, Chan Ghee, Tianning, Tang & Perlin, Marc 2024 An enhanced model for an extreme wave impacting a vertical cylinder. *Coastal Engineering* p. 104630.

Tanimoto, K., Takahashi, S., Kaneko, T. & Shiota, K. 1987 Impulsive Breaking Wave Forces on an Inclined Pile Exerted by Random Waves. In *Coastal Engineering 1986*, pp. 2288–2302. Taipei, Taiwan: American Society of Civil Engineers.

Tassin, Alan, Hulin, Florian & Jacques, Nicolas 2024 A direct multimode method for the reduction of vibration induced oscillations on force signals during "pseudo-rigid" water impact experiments. *Journal of Sound and Vibration* p. 118378.

Wagner, Herbrt 1932 Über Stoß- und Gleitvorgänge an der Oberfläche von Flüssigkeiten. *ZAMM - Journal of Applied Mathematics and Mechanics / Zeitschrift für Angewandte Mathematik und Mechanik* **12** (4), 193–215.

Wienke, J. & Oumeraci, H. 2005 Breaking wave impact force on a vertical and inclined slender pile - theoretical and large-scale model investigations. *Coastal Engineering* **52** (5), 435–462.

Zhang, Nianfan, Xiao, Longfei, Cheng, Zhengshun, Wei, Handi & Chen, Gang 2024 Classification of breaking wave impact loads on a fixed surface-piercing square column with an overhanging deck. *Coastal Engineering* **193**, 104570.

Zhou, D., Chan, E. S. & Melville, W. K. 1991 Wave impact pressures on vertical cylinders. *Applied Ocean Research* **13** (5), 220–234.